First-principles study of spin properties and laser-induced ultrafast spin dynamics in transition-metal oxide clusters $TM_3O_3^{0/+}$ (TM = Fe, Co, and Ni)

Pengpeng Wang,[1] Mingyang Qiu,[1] Xin Lu,[1] Wei Jin,[1,*] Chun Li,[2] Georgios Lefkidis,[2,3,†] and Wolfgang Hübner[3]

[1]*School of Physics and Information Technology, Shaanxi Normal University, Xi'an 710119, China*

[2]*School of Mechanics, Civil Engineering, and Architecture, Northwestern Polytechnical University, Xi'an 710072, China*

[3]*Department of Physics and Research Center OPTIMAS, Technische Universität Kaiserslautern, PO Box 3049, 67653 Kaiserslautern, Germany*

(Received 29 August 2019; revised manuscript received 25 January 2020; accepted 24 February 2020; published 16 March 2020)

We present a first-principles study of spin properties of the triplet $TM_3O_3^{0/+}$ (TM = Fe, Co, Ni) clusters and their laser-induced ultrafast spin dynamics. The differences in geometries, infrared spectra, and level distributions of the three structures are discussed. It is found that the spin localization of the clusters is both structurally and magnetic-field dependent. Specifically, within the same magnetic field, the number of the spin-localized states decreases when the magnetic center changes from Fe via Co to Ni. Even for the same cluster, the spin-localized states may differ under different field directions, due to the fact that spin magnitudes and spin directions of the states change with magnetic field. For the spin dynamics, the results indicate that the system which possesses more spin-localized states normally exhibits rich spin functionalities. Among the various achieved laser-induced ultrafast spin-transfer scenarios, a spin-transfer cycle in Fe_3O_3, a partial demagnetization process in $Co_3O_3^+$, and a spin bifurcation scenario in Ni_3O_3 are presented and analyzed, respectively. These results provide added information for the varieties of ultrafast optical control of magnetism in transition-metal oxide systems, and pave the way toward future related device design and molecular spintronics applications.

DOI: 10.1103/PhysRevB.101.104414

I. INTRODUCTION

Stimulated by the increasing demand for high-density storage and high-speed information processing, optically driven spin dynamics in nanoscale devices within the subpicosecond time regime has become one of the most fascinating topics [1–11] in recent years. Among various kinds of structures (e.g., thin films, alloy multilayers, and bulk materials) where magnetization manipulation has been achieved, molecular clusters/complexes [12–16] offer much promise in future high-density date storage and quantum information processing since they possess ultimate small sizes, long coherence time, and discrete energy levels—the features suitable for scalability and manipulating spin in a controllable and tractable manner. Several spin-based quantum gates and spin functionalities [17–21] in different molecular- or even atomic-scale systems have been proposed, which therefore contribute great steps toward the realization of scalable quantum computing architectures.

As one of the intriguing molecular-scale species, transition metal (TM) oxide clusters have been the subject of numerous experimental and theoretical studies in the last decades due to their great potential applications in catalysis, electronics, and magnetic materials. Various neutral and charged TM_mO_n (TM = Fe, Co, Ni) clusters have been generated by means of laser vaporization techniques [22–24], and their stability, vibrational properties, and structural determination have also been investigated with different tools, such as infrared vibrational spectroscopy and photoionization time-of-flight mass spectrometry [22–31]. In combination with these experiments, a series of density-functional theory calculations concerning the geometric, vibrational, electronic, and magnetic properties of these small clusters have been reported [31–37]. However, most of the studies focus on the ground-state properties and the formation/evolution of nanoparticulate oxides as well as their size-dependent features. The laser-driven ultrafast spin dynamics which usually involves a number of excited states in these clusters, to the best of our knowledge, is rarely investigated.

In the present paper we systematically continue a series of works in which we analyze several aspects regarding the ultrafast magnetization control and logic functionalization of magnetic molecules [21,38–42]. More specifically, here we go a step further and investigate the possible spin manipulation on small $TM_3O_3^{0/+}$ clusters in conjunction with the magnetic anisotropy of the molecules and its relevance to the varieties of achieved spin functionalities. The considerations of choosing such structures are as follows: (1) It has been confirmed by substantial experimental and theoretical work that the small oxide clusters $TM_mO_n^{0/+}$ tend to stabilize preferably with the $n = m$ stoichiometry [22–29]. As elementary entities to assemble hollow tower-like $TM_mO_n^{0/+}$ ($6 \leqslant n \leqslant 12$) structures via vertical stacking, the in-depth study of such existing clusters can not only provide a fundamental understanding of

*jinwei@snnu.edu.cn

†lefkidis@physik.uni-kl.de

ultrafast spin control in small clusters but can also motivate further experimental realization and even the relevant study of larger and more realistic systems. (2) In our previous theoretical study of homodinuclear iron and nickel oxides, it was predicted that ultrafast spin flip (which corresponds to the reversal of spin directions) can be achieved in the FeOOFe and NiOONi clusters, while spin transfer (which corresponds to the change of spin localization) is only possible in FeOOFe [38]. Here, with an additional magnetic center that brings about more *d* electrons, it is expected that the achieved spin dynamics will be richer in types and more novel in features. Especially, as the result will reveal, a reversible spin-transfer cycle is realized in the Fe_3O_3 cluster, which provides more flexibility for constructing practicable, *TM*-based magnetic logic functionality. In addition, their consistent planar geometries can serve as ideal model systems to explore the spin properties of the many-body states of the systems with the change of the magnetic field, and to understand the varieties of the spin functionalities in different structures.

The paper is organized in the following way: In Sec. II the structures and infrared spectra of the three clusters are presented. In Sec. III we demonstrate the magnetic properties of the structures, including the spin magnitudes and directions of the ground states with the change of magnetic field (Sec. III A) and the analysis of the spin localization (Sec. III B). Some selective results of the achieved ultrafast spin dynamics are presented and discussed in Sec. IV. Our summary is given in Sec. V.

II. STRUCTURES AND INFRARED SPECTRA

The clusters are optimized at the Hartree-Fock (HF) level with the Lanl2Dz basis set by using the Gaussian 16 package [43], and their stability is confirmed by the subsequent vibrational harmonic frequency calculation. For the geometries of the three clusters Fe_3O_3, $Co_3O_3^+$ (here, the cationic species is chosen because an even number of electrons enables the separation of charge and spin dynamics), and Ni_3O_3, we restrict ourselves to the planar rings with the oxygen atoms bridging the metal atoms. The reason is that both our own results as well as various other *ab initio* calculations combined with experimental evidence [25–27,30,32–35,44,45] show that they are energetically favored. Regarding their geometries, it turns out that the oxygen atoms preferentially occupy the bridging positions (since the ionic metal-oxygen bonds are stronger than the direct metal-metal bonds) until the number of metal-oxygen bonds is maximized and the whole structures are highly stabilized [25,26,28,30,35].

By performing the calculation under different spin multiplicities and symmetries, we find their ground-state configurations are of spin multiplicities (with symmetries) of 13 (C_s), 11 [26,30,35] (C_{2v}), and 7 [44] (C_s), respectively. Depending on the calculation methods and basis sets applied, other ground-state configurations, for instance, quintet [32,34] and quintet C_s [33] configurations for Fe_3O_3, undectet (i.e., multiplicity 11) D_{3h} [26], triplet [25], and triplet C_{2v} [27] for $Co_3O_3^+$, and triplet Ni_3O_3 [34], are also proposed in some references, which all proved to be higher in energy in our calculation (one exception is the D_{3h} since with this symmetry the calculation does not converge for $Co_3O_3^+$ and always converges to C_s for Fe_3O_3 and Ni_3O_3) than the above ground-state ones.

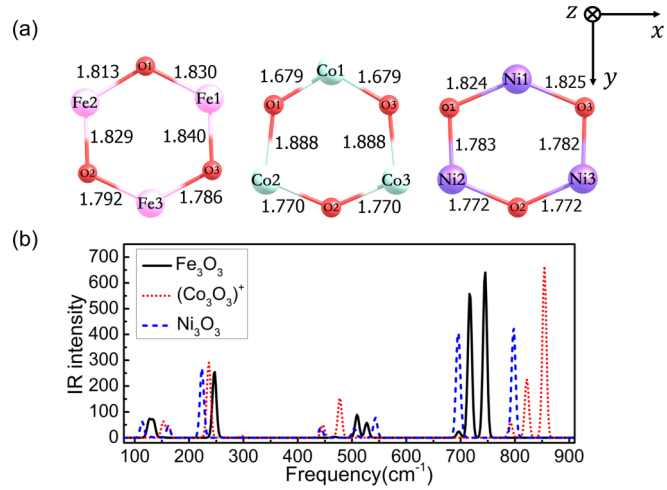

FIG. 1. (a) The optimized planar geometries of triplets Fe_3O_3, $Co_3O_3^+$, and Ni_3O_3 with spin multiplicity 3. The metal-oxide bond lengths (in Å) are shown. (b) The infrared spectra of the three structures.

For the spin dynamics, however, such high ground-state configurations are not feasible due to the huge computational cost (especially for calculation of the excited states) and the limitation of our restricted open-shell HF method for tackling systems with more unpaired electrons (since the restriction of the same spatial orbital for each paired α and β electrons will lead to poor results due to the different effective potentials they experience, especially for the systems with high spin multiplicity). Here, the restricted description is applied since we need reliable spin information (since the unrestricted calculation would cause spin contamination, and give bad results especially for relativistic properties such as the Zeeman interaction parameter *G* tensor [46]). Therefore, considering the acceptable calculation cost and the applied method on the systems, we focus on the triplet configurations (which are lower than the respective singlet ones) to perform spin dynamics.

The optimized planar structures under spin multiplicity 3 together with the metal-oxide bond lengths are shown in Fig. 1(a). Due to the Jahn-Teller effect, the marked bond lengths of each structure are inequivalent (which is similar to the case of Ref. [38]), leading to a reduced symmetry C_s of each structure and making spin localization possible. Among the three clusters, the distortion of the Fe cluster is phenomenologically larger, which can be attributed to the larger energy gained by its less filled *d* electrons through the asymmetrical occupation of the quasidegenerate orbitals. Compared to clusters TM_2O_2 [38], the direct *TM*-O bond lengths of the corresponding $TM_3O_3^{0/+}$ clusters are generally shorter, which is understandable since the trinuclear oxide clusters are more condensed.

The calculated infrared spectra of the three structures, which confirm no imaginary frequencies and prove the geometric stability, are given in Fig. 1(b). The spectra below 100 cm^{-1} are not shown since no vibrational modes with noticeable intensity exist. It can be found that the spectra of the three structures exhibit similar features, except that at high-frequency values (above 600 cm^{-1}) the peaks of the

vibrational modes of $Co_3O_3^+$ are blueshifted and the two peaks of Ni_3O_3 at 695 and 797 cm^{-1} locate farther from each other. In addition, compared to the strong oxide-metal stretching at 704 ± 14 cm^{-1} observed experimentally in the $Co_3O_3^+$ cluster [27], the corresponding peak values of Fe_3O_3 and Ni_3O_3 fall in a reasonable range, while the values of $Co_3O_3^+$ are overestimated in our calculation (the same trend as found in Ref. [27]). Due to the larger number of atoms and stronger bonds of these trinuclear oxide clusters compared to TM_2O_2 clusters [38], the vibrational modes become more, with the main peaks being stronger in intensity and blueshifted.

III. MAGNETIC PROPERTIES OF THE STATES

For the electronic ground and excited states of the structures, to overcome the deficiency of the HF method, we use the symmetry-adapted cluster-configuration interaction (SAC-CI) method [47], which is capable of giving a more accurate description of both the static and dynamic correlations. In addition, to manipulate spin, the degeneracy of the triplet terms needs to be lifted, and the "spin-up" and "spin-down" states should be separated. These are fulfilled by the subsequent inclusion of spin-orbit coupling (SOC, the two-electron contributions of which are accounted for by the effective nuclear charges [48]) and an external magnetic field (B field).

The interaction between laser pulses and molecular systems is described by the time-dependent Hamiltonian $\hat{H}(t) = \hat{\mathbf{D}} \cdot \mathbf{E}_{\text{laser}}(t)$, where $\mathbf{E}_{\text{laser}}(t)$ is the time-dependent electric field of the laser pulses, and $\hat{\mathbf{D}}$ is the electric-dipole transition operator. Here, the laser pulses are chosen as sech^2 shaped and characterized by six parameters, i.e., three angles (θ, ϕ, γ) associated with the direction, energy, pulse duration FWHM, and amplitude [49]. The magnetic dipole interaction $\mu_L \hat{\mathbf{L}} \cdot \mathbf{B}_{\text{laser}}(t) + \mu_S \hat{\mathbf{S}} \cdot \mathbf{B}_{\text{laser}}(t)$ is omitted since usually it is about two orders smaller than the electric dipole interaction [50].

Then, driven by the well-tailored laser pulses and by choosing the appropriate initial and target states with different magnetic properties, certain spin functionalities can be achieved based on the Λ process—an indirect transition channel from the initial state to the final state through the participation of several spin-mixed intermediate states. The time evolution of the system is calculated by solving the following coupled differential equations:

$$i\hbar \frac{\partial c_n(t)}{\partial t} = \sum_k \langle \Phi_n | \hat{H}(t) | \Phi_k \rangle e^{i(E_n - E_k)t/\hbar} c_k(t), \qquad (1)$$

where E_n and E_k are the energies of the unperturbed states $|\Phi_n\rangle$ and $|\Phi_k\rangle$, respectively, and $c_k(t)$ is the time-dependent coefficient of the state $|\Phi_k\rangle$ in the total wave function $\Psi(t) = \sum_k c_k(t) e^{-iE_k t/\hbar} |\Phi_k\rangle$. The time-dependent properties are calculated from their expectation values:

$$\langle \hat{O} \rangle = \sum_{ij} c_i^*(t) c_j(t) O_{ij} = \sum_{ij} P_{ji} O_{ij}, \qquad (2)$$

where $P_{ij} = c_j^*(t) c_i(t)$ are the density matrix elements, and $O_{ij} = \langle \Phi_i | \hat{O} | \Phi_j \rangle$ are the matrix elements in the basis of the unperturbed Hilbert space. More theoretical details can be found in Refs. [38,39,51].

As illustrated in our previous work [21,39–41], the most basic functional elements for constructing logic operations are spin-flip (for storage) and spin-transfer (for logic) scenarios. Especially for spin transfer, it is only meaningful when changing the spin localization between different centers, and in most cases only possible under an appropriate magnetic field direction. Therefore, before presenting the spin dynamics in detail, we would like to demonstrate the magnetic properties of the many-body states of the three triplet structures, i.e., the B-field-dependent spin magnitudes and directions (Sec. III A) and some analysis of the spin localization (Sec. III B). These features can help us to understand the fact that spin states change with different B fields and why the achieved spin functionalities are both structurally and field dependent from the viewpoint of spin localization. Recently, the magnetic anisotropy in magnetic molecular systems has been investigated (through the zero-filed splitting parameter D and Zeeman interaction parameter G) [46,52], which from another point of view also provides valuable information to uncover the nature of the electronic states.

Note that throughout the paper for the many-body states and for the subsequent spin dynamics, we only consider the Fock space which includes the lowest 61 states (numbered by the order of their energies, the level diagram under a certain B-field direction for each structure can be seen in Sec. IV). This means that for each structure the ten lowest triplet terms before the inclusion of SOC for each irreducible representation are calculated with the SAC-CI method; thus within the point group of C_s, there are in total 60 triplet states, in addition to the one singlet SAC state. Regarding the control of the coherent magnetization we only report the spin dynamics, due to the fact that the orbital angular momentum in our systems is usually partially or completely quenched (due to the lifting of the d-orbital degeneracy). Interestingly, we find that most of the 61 calculated electronic states for each structure have very small orbital-angular momentum expectation values. Specifically in Ni_3O_3 (to mention an example), merely six states have values above 0.2.

A. Magnetic-field-dependent spin magnitudes and spin directions of the triplet ground states

Since the three clusters are all planar structures, it is feasible and straightforward to investigate the changes of spin magnitudes $|S|$ (i.e., $\sqrt{\langle S_x \rangle^2 + \langle S_y \rangle^2}$) and directions $\arctan(\langle S_y \rangle / \langle S_x \rangle)$ by scanning all the B-field directions in the x-y plane with different field magnitudes. The results for the ground states of the three triplet structures are shown in Fig. 2, in which the diagram of $|S|$-Φ is plotted in a polar form, and $\arctan(\langle S_y \rangle / \langle S_x \rangle)$-$\Phi$ is a Cartesian plot. Here, the direction of the B field in the x-y plane is denoted by (Θ, Φ), where the polar angle Θ is 90°, and the azimuthal angle Φ is the angle of the B field that deviates from the x axis. Clearly, from Figs. 2(a1)–2(a3) we see that the in-plane easy axes (in which directions the values of spin magnitude are maxima) of Fe_3O_3, $Co_3O_3^+$, and Ni_3O_3 are different. The directions of them are approximately $(\Theta, \Phi) = (90°, 120°)$ [or $(90°, 300°)$], $(\Theta, \Phi) = (90°, 0°)$ [or $(90°, 180°)$], and $(\Theta, \Phi) = (90°, 82.5°)$ [or $(90°, 262.5°)$], respectively. They can be also determined by the polar plots of energy shifting

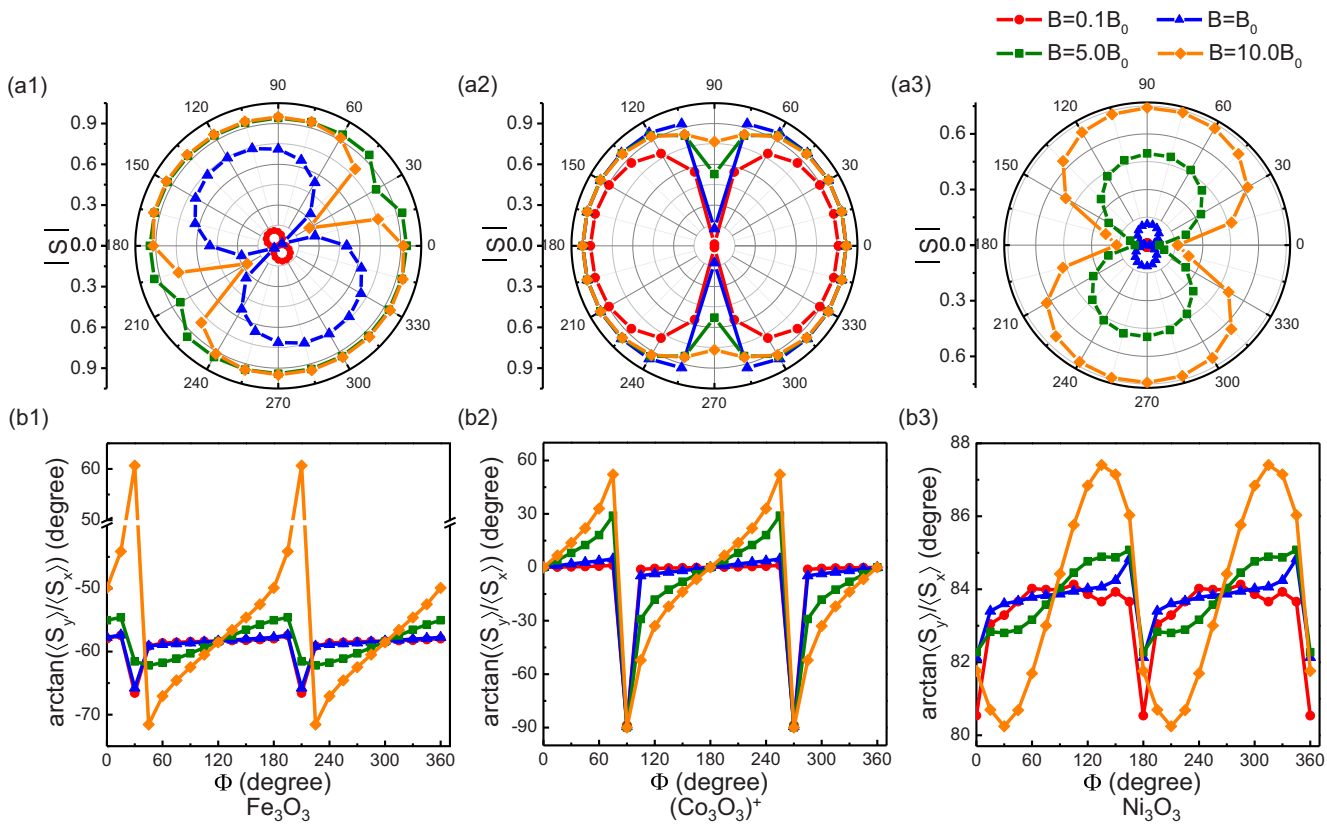

FIG. 2. The spin magnitudes and directions for the ground states of the three structures for different B-field directions in the molecular plane [denoted by (90°, Φ)] with four different field strengths. (a1), (a2), and (a3) are the polar plots of the spin directions as functions of B for the ground states of Fe_3O_3, $Co_3O_3^+$, and Ni_3O_3, respectively. (b1), (b2), and (b3) are the normal Cartesian plots of spin directions with the change of B for the ground states of Fe_3O_3, $Co_3O_3^+$, and Ni_3O_3, respectively. The four field strengths are $0.1B_0$ (circles), B_0 (triangles), $5B_0$ (squares), and $10B_0$ (diamonds) with $B_0 = 10^{-5}$ a.u. = 2.35 T.

of the ground states with respect to Φ, which gives the same result, as shown in Fig. 4 in the Appendix. Clearly, as the B-field strength increases, the spin magnitude of the ground state for each cluster, which shows a twofold-like symmetry, generally becomes larger under each specific field direction. Here, it is obvious that the responses of the three clusters (at least for their ground states) to the B-field strength are not synchronous, which can be directly seen from Fig. 5 in the Appendix, in which the ground-state spin magnitude of each cluster in the direction of the in-plane easy axis with the change of B-field strength is plotted.

Figures 2(b1)–2(b3) show the corresponding spin directions with the changes of B. Clearly, with the increase of the B-field strength, the slope of the spin direction $\arctan(\langle S_y\rangle/\langle S_x\rangle)$ of the ground state for each triplet cluster gradually gets larger, reflecting the trend that the spin direction turns toward the field direction. This is particularly noticeable for the case of $Co_3O_3^+$ when $|B| = 10B_0 = 23.5$ T, since the linear fitting of the change trends of the spin angles in the range of [90°–255°] for Φ gives a slope of 0.7 and a phase difference of −126.5°, which is close to the extreme situation where the spin direction is exactly in tune with the field direction (i.e., a slope of 1.0 with the phase difference −180°). Here, due to the fact that the magnetic field strength in our calculation is in atomic units, their different values for investigating the B-field-dependent properties in this paper are chosen as multiples of B_0, where $B_0 = 10^{-5}$ a.u. = 2.35 T. From Fig. 2 one can find that, among the the three clusters, $Co_3O_3^+$ is the easiest one to get magnetized due to its relatively large spin magnitudes and most sensitive response to the B-field direction, Ni_3O_3 is the hardest one, and Fe_3O_3 lies in-between. This is confirmed from the result of magnetization curves of the three clusters as shown in Fig. 5 in the Appendix. Note that the two abrupt drops (or rises) of $\arctan(\langle S_y\rangle/\langle S_x\rangle)$ for each line in Figs. 2(b1)–2(b3) indicate the angles where phase transitions of spin directions occur, which approximately correspond to the in-plane hard axes for all the three clusters.

It should be clarified that the aforementioned in-plane easy and in-plane hard axes are named from the comparison of the spin magnitudes when the B field changes within the molecular plane. For the determination of the global easy and hard axes of the three clusters, we need to scan all the other possible B-field directions beyond the molecular plane. The results (see Fig. 6 in the Appendix) show that the global easy and hard axes of Ni_3O_3 are exactly the in-plane ones, while for Fe_3O_3 and $Co_3O_3^+$, their global easy axes are the same as the in-plane ones, but the global hard axes become almost collinear with the z axis. In addition, we emphasize here that the results shown in Fig. 2 are only for the ground states; the easy axes do not represent the directions chosen for the spin dynamics to be discussed later since the dynamics usually involves many excited states and the easy axis for each state

TABLE I. The distribution (i.e., the percentage values of certain states out of total 61 states) of the spin localized or unlocalized states of the three structures under three typical B-field directions (with strength of 10^{-5} a.u.), as well as the correspondingly achieved spin functionalities. Here, the abbreviation S represents spin localization in one single magnetic atom, D/T means spin localization in two or three magnetic centers simultaneously, and N means no spin localization.

	Fe_3O_3				$Co_3O_3^+$				Ni_3O_3			
B field	S (%)	D/T (%)	N (%)	Spin functionality	S (%)	D/T (%)	N (%)	Spin functionality	S (%)	D/T (%)	N (%)	Spin functionality
$(0, 0, B_z)$	26.2	16.4	57.4	Flip in Fe1/2/3 Transfer cycle[a]	–	39.3	60.7	Global flip Partial demagnetization	9.9	9.9	80.2	Flip in Ni1/2/3 Transfer (one)
$(B_x, 0, 0)$	42.6	16.4	41.0	Flip in Fe1/2/3 Transfer cycle[b] Transfer (two extra)	–	36.1	63.9	Global flip	6.6	18.0	75.4	–
$(0, B_y, 0)$	36.1	18.0	45.9	Flip in Fe2 Transfer (two)	–	26.2	73.8	Global flip	6.6	18.0	75.4	Flip in Ni1 Bifurcation

[a]A sequential transfer cycle which involves three initial/final states: Fe2 (state $|25\rangle$) → Fe1 (state $|38\rangle$) → Fe3 (state $|56\rangle$) → Fe2 (state $|25\rangle$).
[b]A transfer cycle which involves five initial/final states: Fe1 (state $|19\rangle$) → Fe2 (state $|23\rangle$), Fe2 (state $|42\rangle$) → Fe3 (state $|33\rangle$), Fe3 (state $|33\rangle$) → Fe1 (state $|36\rangle$).

may be different. For instance, for the two initial/final states $|25\rangle$ and $|38\rangle$ of the spin-transfer cycle achieved in Fe_3O_3 when B is along the z axis (Sec. IV), the global easy axis of state $|25\rangle$ is $(\Theta, \Phi) = (90^\circ, 30^\circ)$ [or $(90^\circ, 210^\circ)$], exactly the in-plane hard axis of the ground state, and the global easy axis of $|38\rangle$ is the z axis.

B. Spin localization analysis

Table I lists the distribution of spin-localized or spin-nonlocalized states of each cluster under three different typical B fields as well as the achieved spin functionalities. Here for the strength of the B field applied in the spin dynamics, the value of 2.35 T (i.e., B_0) is chosen. It should be noted that the spin-localized and -nonlocalized states are clarified by the expectation values of the spin components (the maximum of which is 1.00) and spin-density values (or the sum of the values in two or three magnetic centers, the maximum of which is 2.00). That is, when the two values of a certain state are above 0.40 (for reasons of experimental detectability) and 0.80 (which is almost one half of the maximum total density), respectively, we name it a spin-localized state; otherwise it is a spin-nonlocalized state.

It is found that the spin localization of the states is both structurally and B-field dependent. For the structural effect, within the same B field, the number of spin-localized states decreases when the magnetic center changes from Fe via Co to Ni, which can be seen from the increasing values of the non-localized percentage values (e.g., 57.4%, 60.7%, and 80.2% for the case of the B field being along the z axis). This can be analyzed from their geometry. Generally, the more distorted the structure is, the more distinct spin localization it has. Among the three structures, Fe_3O_3 is the most asymmetric one (although it belongs to the same point group as the other two clusters) with respect to the obvious inequivalence of the Fe-O bond lengths; thus the three magnetic centers can be well distinguished and possess the most spin-localized states. For $Co_3O_3^+$ and Ni_3O_3, with respect to the TM1-O2 bond, the direct TM-O bonds in the left part of each cluster are almost the same as the corresponding ones in the right part; thus most of the states either have spin localization equally in two/three magnetic centers or have no spin localization. Especially for the cluster $Co_3O_3^+$ where the differences between the left-side and right-side TM-O bonds are the least, none of the states has spin localized in one single magnetic atom. This is consistent with the findings in Ref. [38]. It has been shown that the magnetic moments of oxygen in $Fe_xO_y^{0/+}$ clusters may show unusually strong spin polarization [37]. Here for the three triplet homotrinuclear clusters, at least within the Fock subspace we investigate, there is no strong spin localization on oxygen atoms. However, according to our ongoing study, oxygen can be considered as a magnetic center for some excited states of the heterotrinuclear ones (e.g., $Fe_2CoO_3^+$, $Ni_2CoO_3^+$, and $FeCoNiO_3^+$) due to the its large spin-density values.

For the B-field effect, the spin-localized states of Fe_3O_3 and $Co_3O_3^+$ when B is along the x axis are more than those when B is along the y axis, since the B field along the x axis breaks the structural "mirror" symmetry (with respect to the Fe3-O1 or Co1-O2 bond) more significantly than parallel to the y axis. Similarly, the spin-localized states of Fe_3O_3 and Ni_3O_3 when the B field is parallel to the molecular plane (i.e., along the x or y axis) are more than the ones when the field is perpendicular to the molecular plane (i.e., along the z axis). These differences are also quite understandable from our analysis in the the previous subsection: Since different B-field directions may lead to different spin magnitudes (or expectation values of the spin components), it may occur that some spin-localized (-nonlocalized) states under one B-field direction become unlocalized (spin-localized) under another direction, due to the substantial decreases (increases) of the corresponding spin values.

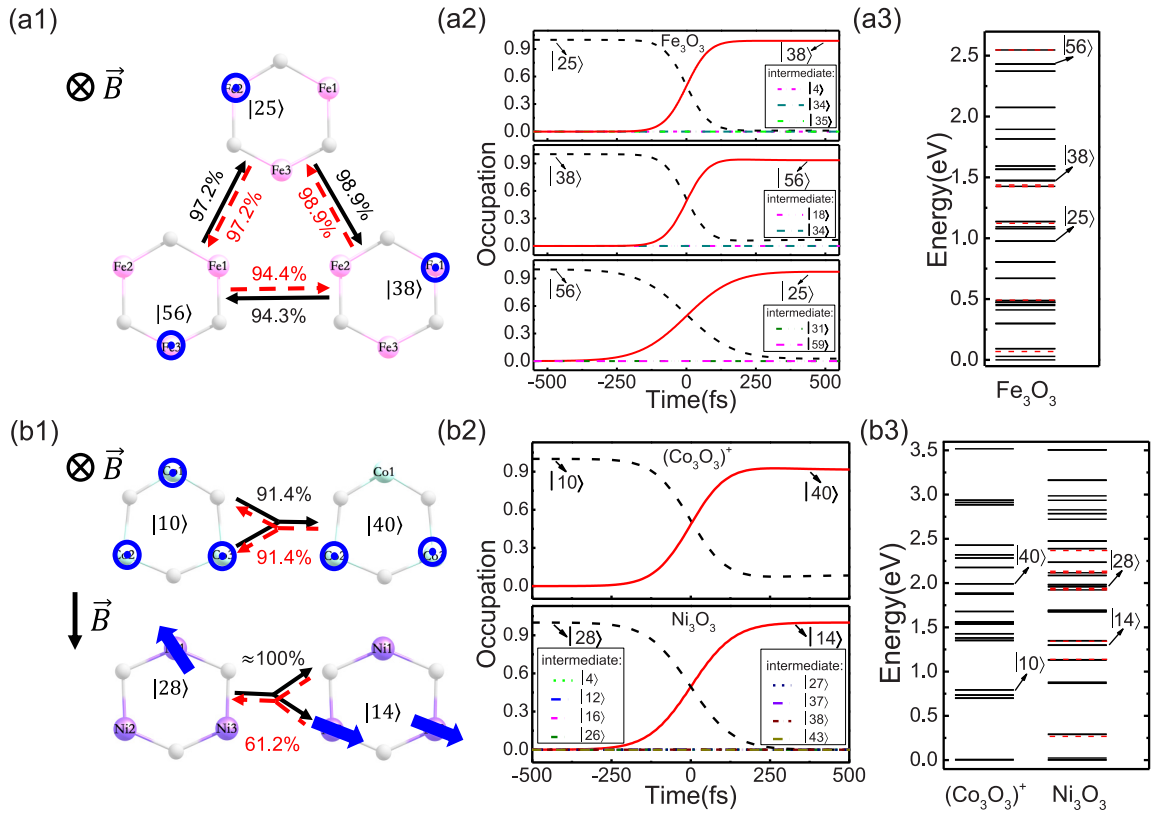

FIG. 3. The ultrafast spin dynamics achieved in the three triplet clusters. (a1) and (b1) Schematic illustration of the spin-transfer cycle, the partial demagnetization, and the spin bifurcation in Fe_3O_3, $Co_3O_3^+$, and Ni_3O_3, respectively. The inside-out oriented or broad arrows on the magnetic centers denote spin directions, and the percentage values beside the solid and dashed thin arrows between different configurations denote the fidelity of the transfer processes. (a2) and (b2) The time-resolved occupations of the involved states (initial state: black dotted, final state: red solid, intermediate states: others) for each scenario. (a3) and (b3) The energetic positions of the involved states (dashed are intermediate states).

Correspondingly, the achieved spin functionalities, apart from the cause of the distinct nature of the systems, are also to some extent subjected to the field directions (as shown in Table I). This is because the change of B-field direction can bring about different spin directions and localization for some states, affect the choice of the candidate initial and final states for a certain spin function, and may also change the selection rules between them within the electric dipole approximation. Nevertheless, it is expected that the cases with more spin-localized states will provide us more flexibilities to achieve the desired spin dynamics. For instance, as can be seen in Table I, the achieved spin functionalities in Fe_3O_3 are richer than those obtained in $Co_3O_3^+$ and Ni_3O_3. Interestingly, when the B field is along the z axis, we achieve a spin-transfer cycle which only involves three initial/final states. This sequential cycle can be easily controlled in experiment and is promising in the future application of spin shift register [17]. In addition, compared to the traditional spin transfer, we achieve one partial demagnetization scenario (for the case when the B field is along the z axis) and one spin bifurcation scenario (for the case when the B field is along the y axis) in $Co_3O_3^+$ and Ni_3O_3, respectively. These scenarios are significant for constructing spin logic functionality. Therefore, in the next section, we will present the dynamics results of the three types of spin functionalities and inspect their underlying physics, in the hope of providing some rules of thumb and guidance for the future experimental realization and device design.

IV. LASER-INDUCED ULTRAFAST SPIN DYNAMICS

As mentioned in our previous discussion, for the case when the B field is along the z axis (the coordinate system is referred in Fig. 1), a spin-transfer cycle, i.e., Fe2 (state $|25\rangle$) $\rightarrow$ Fe1 (state $|38\rangle$) $\rightarrow$ Fe3 (state $|56\rangle$) $\rightarrow$ Fe2 (state $|25\rangle$), is achieved in Fe_3O_3 [as shown in Figs. 3(a1) and 3(a2)]. The fidelity (which is the occupation of the desired final state) of each scenario is 98.9%, 94.3%, and 97.2%, respectively, contributing a total efficiency of 90.7%. The energies, spin expectation values, spin density, and spin localization of the three initial/final states are listed in Table II. The energetic positions of the initial and final states are clearly indicated in the levels of Fe_3O_3, as shown in Fig. 3(a3). As indicated in Fig. 3(a2), there are only three, two, and two intermediate states, respectively, involved in each scenario, which makes the dynamics behave relatively simply and efficiently [42]. The energetic positions of these intermediate states are marked with dashed lines in Fig. 3(a3). Detailed inspection

TABLE II. Information of the initial and final states (including their energies, spin expectation values, spin density, and spin localization) for the spin scenarios presented in this paper. Here *TM* refers to the Fe, Co, or Ni center depending on the structure discussed.

Structure	Initial/final states	Energy (eV)	$\langle S_x \rangle$	$\langle S_y \rangle$	$\langle S_z \rangle$	Spin density *TM*1	Spin density *TM*2	Spin density *TM*3	Localization
Fe_3O_3,	$\|25\rangle$	0.97	0.00	0.00	−0.50	0.03	0.98	0.02	Fe2
$\mathbf{B} = (0, 0, B_z)$	$\|38\rangle$	1.47	0.00	0.00	−0.86	1.71	0.03	0.06	Fe1
	$\|56\rangle$	2.43	0.00	0.00	−0.87	0.08	0.19	1.49	Fe3
$Co_3O_3^+$,	$\|10\rangle$	0.79	0.00	0.00	−0.62	0.73	0.52	0.52	Co1 + Co2 + Co3
$\mathbf{B} = (0, 0, B_z)$	$\|40\rangle$	1.99	0.00	0.00	−0.57	0.08	0.83	0.84	Co2 + Co3
Ni_3O_3,	$\|14\rangle$	1.30	0.48	0.10	0.00	0.09	0.26	0.64	Ni2 + Ni3
$\mathbf{B} = (0, B_y, 0)$	$\|28\rangle$	1.96	−0.25	−0.55	0.00	0.95	0.01	0.02	Ni1

of the absorption of the three initial/final states shows that for each scenario the involved intermediate states have both comparable transition peaks with the initial and final states, thus indicating the transferability of the whole cycle. The laser parameters of the three sequential scenarios are given in Table III. As it shows, the laser energies for driving the three scenarios are 0.50, 0.95, and 1.46 eV, respectively, which are almost resonant to the respective energy differences between the initial and final states in each scenario (i.e., $\Delta E_{38,25} = 0.50$ eV, $\Delta E_{56,38} = 0.96$ eV, $\Delta E_{56,25} = 1.46$ eV). This can occur in the Λ-process-based transfer scenario where the initial and final states are neither too far (e.g., above 5.9 eV) nor too close (e.g., less than 0.03 eV); otherwise a combination of several multiphoton processes will take place [41] or the laser energy will be determined more or less as the energy difference between the initial/final and (most probably the farthest) intermediate states [42,53]. For these three scenarios, the larger the energy difference between the initial and final states, the higher the laser energy the process requires. In addition, a large energy difference can also slow down the dynamics, making the dynamics $|56\rangle \rightarrow |25\rangle$ being the longest. What is more, we find that when we exchange the initial and final states of each scenario and apply the same respective laser pulses, all three scenarios are reversible. The fidelity of each reversed process is almost equivalent to that of the original one. We attribute this reversibility to the small number of intermediate states involved and the symmetric dynamical behavior of the scenarios, as demonstrated in Ref. [42]. It should be noted that when the B field is along the x axis, a spin-transfer cycle is also achieved, but with five initial/final states [Fe1 (state $|19\rangle$) → Fe2 (state $|23\rangle$), Fe2 (state $|42\rangle$) → Fe3 (state $|33\rangle$), Fe3 (state $|33\rangle$) → Fe1 (state $|36\rangle$)], which experimentally is harder to control compared to the present one.

For $Co_3O_3^+$ and Ni_3O_3, since the states of them with spin localization in single magnetic atoms are much less than those in Fe_3O_3, spin-transfer cycles have not been found. In addition, the spin-transfer scenarios from one single magnetic center to another single magnetic center are also less (only one transfer scenario can be achieved in Ni_3O_3 when the B field is along the z axis, as shown in Table I). Interestingly, we achieve a partial demagnetization scenario (spin transfer from state $|10\rangle$ with spin equally distributed in three cobalt atoms to state $|40\rangle$ with spin localization in both Co2 and Co3) in $Co_3O_3^+$ and a spin bifurcation one (spin transfer from state $|28\rangle$ with spin localization in Ni1 to state $|14\rangle$ with spin localization in Ni2 and Ni3) in Ni_3O_3 by applying the B field along the z axis and along the y axis, respectively. The former is a direct process without any intermediate states involved, and the latter one is a Λ process where there are eight intermediate states participating. The dynamics is shown in Figs. 3(b1) and 3(b2). The corresponding fidelity is 91.4% and almost 100%, respectively. The initial and final states of the two scenarios are indicated in their respective SAC-CI level diagrams [Fig. 3(b3)], of which the energies, spin expectation values, spin density values, and spin localization are listed in Table II. Clearly, due to the cooperative effects of different atomic species and different numbers of electrons and basis functions, the levels of these two structures, with larger energy gaps, expand more broadly than Fe_3O_3.

TABLE III. The optimized parameters of the laser pulses for the achieved ultrafast spin dynamics scenarios. Here, θ and ϕ denote the angles of the incidence in spherical coordinates, and γ is the angle between the polarization of the light and the optical plane. FWHM is the full width at half maximum of the laser pulse.

Structure	Process	Laser parameters θ (deg)	ϕ (deg)	γ (deg)	Amplitude (a.u.)	FWHM (fs)	Energy (eV)
Fe_3O_3, $\mathbf{B} = (0, 0, B_z)$	$\|25\rangle \leftrightarrow \|38\rangle$	136.0	227.3	1.7	0.004	222.1	0.50
	$\|38\rangle \leftrightarrow \|56\rangle$	170.1	229.8	227.8	0.006	223.4	0.95
	$\|56\rangle \leftrightarrow \|25\rangle$	179.9	117.1	359.1	0.002	468.1	1.46
$Co_3O_3^+$, $\mathbf{B} = (0, 0, B_z)$	$\|10\rangle \leftrightarrow \|40\rangle$	163.0	34.6	115.3	0.007	317.1	1.20
Ni_3O_3, $\mathbf{B} = (0, B_y, 0)$	$\|28\rangle \rightarrow \|14\rangle$	144.1	207.0	160.1	0.007	369.1	0.66

It is found that the laser energy for driving the bifurcation of Ni_3O_3 is lower than that for driving the partial demagnetization in $Co_3O_3^+$ (as can be seen in Table III). In addition, the FWHM is a little larger than that of $Co_3O_3^+$, indicating the fact that more intermediate states may slow down the dynamics process. However, the most obvious effect of the intermediate states is that they decrease the efficiency of the reversed process in Ni_3O_3. As shown in Fig. 3(b1), by using the same laser parameters for the spin bifurcation of Ni_3O_3, its reversed process, i.e., spin transfer from state $|14\rangle$ to state $|28\rangle$, achieves only a 61.2% fidelity, in which case we name it a quasireversible process. This might be used for the ERASE functionality [21] or for preparing a specific state as the initial state. About the quasireversibility, our study shows that, with the involvement of 14 intermediate states for the reversed process, the system goes over to a linear combination of states $|28\rangle$ and $|13\rangle$ with final occupations 61.2% and 36%, respectively. This indicates that the initially occupied state has been partially merged and partially flipped (since state $|13\rangle$ stems from the same triplet term as state $|14\rangle$ but with opposite spin direction). The latter occupation is also close to the fidelity 42.7% of the spin flip from state $|14\rangle$ to state $|13\rangle$, for which most of the intermediate states coincide with the aforementioned 14 intermediate states.

V. SUMMARY

Using high-level quantum chemistry calculations, we investigate the structures, infrared spectra, and spin properties of triplet $TM_3O_3^{0/+}$ (TM = Fe, Co, Ni) clusters, and predict various ultrafast laser-induced spin dynamics scenarios. The following conclusions can be drawn.

(i) The spin properties of the structures change with the B field. For the ground states of the three clusters, the in-plane easy axes, determined from the spin magnitudes or the ground-state energies by scanning all the B-field directions within the molecular plane, are found to be different. When increasing the strength of the B field, the spins tend to align with its direction. It turns out that the $Co_3O_3^+$ cluster is the easiest one to be magnetized due to its relatively large spin magnitudes and most sensitive response to the B-field direction, Ni_3O_3 is the hardest one, and Fe_3O_3 lies in between, which is also confirmed from their respective magnetization curves.

(ii) The spin localization of the clusters is both structural and B-field-direction dependent. For the structural effect, within the same B field, the amount of spin-localized states follows the order Fe > Co > Ni. It is found that normally the more spin-localized states the system possesses, the more spin functionalities it supports. For the B-field effect, since spin magnitudes and directions are subjected to the B-field direction, the spin-localized states of the same cluster under different field directions may be different. It turns out that the spin-localized states of Fe_3O_3 and $Co_3O_3^+$, when the B field is along the x axis, are more than those when the B field is along the y axis, and the spin-localized states of Fe_3O_3 and Ni_3O_3 when the B field is parallel to the molecular plane are more numerous than when the field is perpendicular to it, which

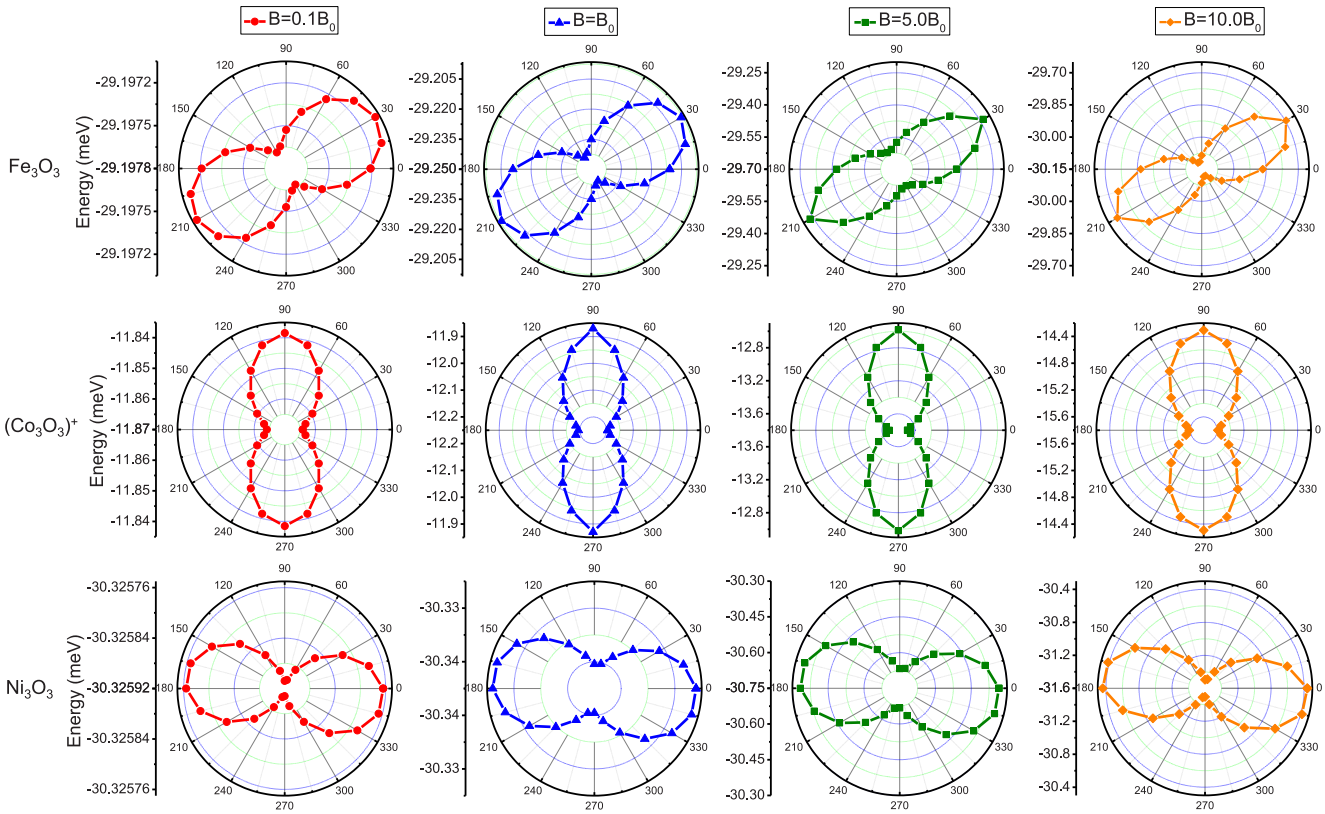

FIG. 4. The polar plots of the ground-state energy shifting of the three structures under different B-field directions in the molecular plane [denoted by $(90^\circ, \Phi)$] with four different field strengths of $0.1B_0$ (circles), B_0 (triangles), $5B_0$ (squares), and $10B_0$ (diamonds).

can be attributed to the fact that the former B-field direction in each case breaks the structural symmetry more significantly.

(iii) Among the various achieved laser-induced ultrafast spin-transfer dynamics, a spin-transfer cycle in Fe_3O_3, a partial demagnetization process in $Co_3O_3^+$, and a spin bifurcation scenario in Ni_3O_3 are presented and analyzed, respectively. It is found that the smaller the number of the intermediate states involved, the easier for the dynamics to go backward under the same laser pulses. Due to the well-localized and evenly distributed spin states, we conclude that the iron-containing clusters have more extensive applications and greater potential in future logic operations because it is easier to control their spin and exhibit more spin functionalities.

These results provide a deep insight into the spin properties of the trinuclear transition-metal oxides and help to understand the varieties of ultrafast spin functionalities in them and even larger *TM* oxide systems. It is expected that the present investigation will stimulate the realization of these prospective functionalities and serve as a useful reference for the related molecular spintronics device applications in the future.

ACKNOWLEDGMENTS

We acknowledge financial support from the National Natural Science Foundation of China (Grants No. 11504223, No. 11872309, and No. 11572251), the Natural Science Basic Research Plan in Shaanxi Province (Grant No. 2017JM1033), and the Fundamental Research Funds for the Central Universities (Grants No. GK201903015 and No. 3102017JC01003).

APPENDIX

As stated in the text, the in-plane easy and hard axes can also be determined from the energy shifting of the ground states of the three clusters with the change of Φ, which is detectable in experiment. The results under four different B-field strengths for each cluster are given in Fig. 4, from which one can clearly see that the in-plane easy (the directions where the shifting values are lowest) and hard (the directions where the shifting values are the highest) axes are the same as the ones obtained in Figs. 2(a1)–2(a3). Here, the plots for each structure are split into four subfigures for reasons of distinguishability.

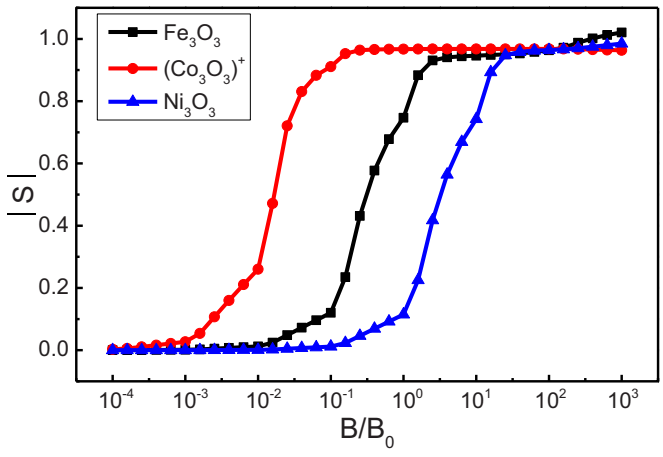

FIG. 5. The spin magnitudes for the ground states of the three clusters for different B-field strengths B/B_0 along the directions of their respective in-plane easy axes [i.e., $(\Theta, \Phi) = (90^\circ, 120^\circ)$ for Fe_3O_3, $(\Theta, \Phi) = (90^\circ, 0^\circ)$ for $Co_3O_3^+$, and $(\Theta, \Phi) = (90^\circ, 82.5^\circ)$ for Ni_3O_3].

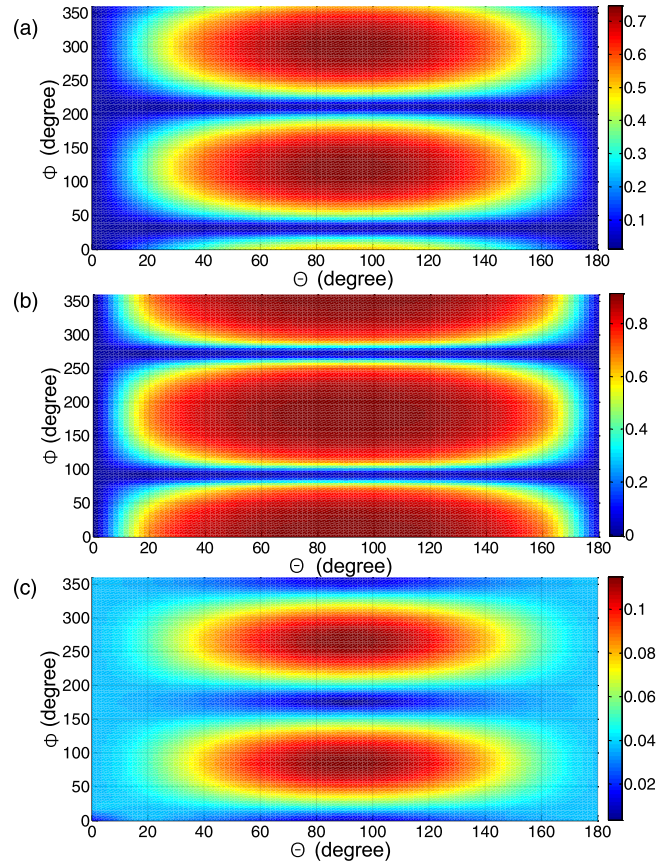

FIG. 6. The spin magnitudes for the ground states of the three clusters for different B-field directions. The B-field strength is chosen as $0.1B_0$ for $Co_3O_3^+$ and B_0 for Fe_3O_3 and Ni_3O_3.

To understand why the spin magnitudes for the ground states of the three clusters are markedly different and the spin directions follow different paces under the same B-field strength as shown in Fig. 2, we plot the magnetization trends under different B-field strengths in the directions of their respective in-plane easy axes. The results are given in Fig. 5. Clearly, the responses of the three clusters in their ground states to the field strength are asynchronous. Specifically, the ground state of $Co_3O_3^+$ turns out to be the easiest one to get magnetized even under small B-field strength since it can be almost saturated at the field strength of $0.1B_0$. This can be also seen from the overall large spin magnitudes in Fig. 2(a2) under the four different B-field strengths and the almost linear dependence of its spin directions on the B-field direction for B equal to $10B_0$ in Fig. 2(b2). For the ground state of Ni_3O_3, the threshold B-field strength for its saturation is around $10B_0$, and thus is considered as the most difficult one. For Fe_3O_3, the threshold B-field strength for saturation lies in between. Again, we emphasize that these are only for the ground states; they do not represent the trends of their excited states.

By scanning all the possible B-field directions, the global easy and hard axes of the ground states of the three clusters can be determined. The results under the B-field strength of $0.1B_0$ for $Co_3O_3^+$ and B_0 for Fe_3O_3 and Ni_3O_3 are shown in Fig. 6, from which one can promptly see the approximate global easy and hard axes: The global easy axes (which correspond to the directions where the spin magnitudes are maxima) of Fe_3O_3, $Co_3O_3^+$, and Ni_3O_3 are around $(\Theta, \Phi) = (90^\circ, 120^\circ/300^\circ)$, $(\Theta, \Phi) = (90^\circ, 0^\circ/180^\circ)$, and $(\Theta, \Phi) = (90^\circ, 82.5^\circ/262.5^\circ)$, respectively, and the hard axes (which correspond to the directions where the spin magnitudes are minima) are around the z axis, z axis, and $(\Theta, \Phi) = (90^\circ, 172.5^\circ/352.5^\circ)$, respectively.

Here, since the directionally dependent changes of spin magnitudes for $Co_3O_3^+$ under the B-field strength of B_0 are not clear enough to resolve [e.g., the circle-shaped $|S|$-Φ plot in Fig. 2(a2)], it is not reliable to determine its global easy and hard axes under such a saturated B-field strength (which is also true for the cases of Fe_3O_3 and Ni_3O_3 under the field strength equal to or larger than $10B_0$ and $50B_0$, respectively). Thus, a moderate strength of $0.1B_0$ is chosen for $Co_3O_3^+$ in Fig. 6. Actually, the easy/hard axis of each cluster is always the same when choosing smaller field strength, e.g., for the cases of the strength equal or smaller than $10B_0$, $0.5B_0$, and $50B_0$ for Fe_3O_3, $Co_3O_3^+$, and Ni_3O_3, respectively.

[1] E. Beaurepaire, J.-C. Merle, A. Daunois, and J.-Y. Bigot, Phys. Rev. Lett. **76**, 4250 (1996).

[2] G. P. Zhang and W. Hübner, Phys. Rev. Lett. **85**, 3025 (2000).

[3] C. D. Stanciu, F. Hansteen, A. V. Kimel, A. Kirilyuk, A. Tsukamoto, A. Itoh, and T. Rasing, Phys. Rev. Lett. **99**, 047601 (2007).

[4] A. Kirilyuk, A. V. Kimel, and T. Rasing, Rev. Mod. Phys. **82**, 2731 (2010).

[5] U. Atxitia and O. Chubykalo-Fesenko, Phys. Rev. B **84**, 144414 (2011).

[6] B. Pfau, S. Schaffert, L. Müller, C. Gutt, A. Al-Shemmary, F. Büttner, R. Delaunay, S. Düsterer, S. Flewett, R. Frömter *et al.*, Nat. Commun. **3**, 1100 (2012).

[7] T. Roth, A. J. Schellekens, S. Alebrand, O. Schmitt, D. Steil, B. Koopmans, M. Cinchetti, and M. Aeschlimann, Phys. Rev. X **2**, 021006 (2012).

[8] A. Eschenlohr, M. Battiato, P. Maldonado, N. Pontius, T. Kachel, K. Holldack, R. Mitzner, A. Föhlisch, P. M. Oppeneer, and C. Stamm, Nat. Mater. **12**, 332 (2013).

[9] V. Shokeen, M. Sanchez Piaia, J.-Y. Bigot, T. Müller, P. Elliott, J. K. Dewhurst, S. Sharma, and E. K. U. Gross, Phys. Rev. Lett. **119**, 107203 (2017).

[10] O. Morandi and P.-A. Hervieux, Phys. Rev. B **96**, 024441 (2017).

[11] C. Li, J. Liu, S. B. Zhang, G. Lefkidis, and W. Hübner, Carbon **87**, 153 (2015).

[12] W. Wernsdorfer, Int. J. Nanotechnol. **7**, 497 (2010).

[13] S. Sanvito, Chem. Soc. Rev. **40**, 3336 (2011).

[14] O. Diéguez, M. M. G. Alemany, C. Rey, P. Ordejón, and L. J. Gallego, Phys. Rev. B **63**, 205407 (2001).

[15] G. L. Gutsev and C. W. Bauschlicher, J. Phys. Chem. A **107**, 7013 (2003).

[16] M. Stamenova, J. Simoni, and S. Sanvito, Phys. Rev. B **94**, 014423 (2016).

[17] G. D. Mahan, Phys. Rev. Lett. **102**, 016801 (2009).

[18] A. A. Khajetoorians, J. Wiebe, B. Chilian, and R. Wiesendanger, Science **332**, 1062 (2011).

[19] W.-H. Soe, C. Manzano, A. De Sarkar, F. Ample, N. Chandrasekhar, N. Renaud, P. de Mendoza, A. M. Echavarren, M. Hliwa, and C. Joachim, Phys. Rev. B **83**, 155443 (2011).

[20] F. Luis, A. Repollés, M. J. Martínez-Pérez, D. Aguilà, O. Roubeau, D. Zueco, P. J. Alonso, M. Evangelisti, A. Camón, J. Sesé, L. A. Barrios, and G. Aromi, Phys. Rev. Lett. **107**, 117203 (2011).

[21] C. Li, S. B. Zhang, W. Jin, G. Lefkidis, and W. Hübner, Phys. Rev. B **89**, 184404 (2014).

[22] D. N. Shin, Y. Matsuda, and E. R. Bernstein, J. Chem. Phys. **120**, 4150 (2004).

[23] D. N. Shin, Y. Matsuda, and E. R. Bernstein, J. Chem. Phys. **120**, 4157 (2004).

[24] K. S. Molek, C. Anfuso-Cleary, and M. A. Duncan, J, Phys. Chem. A **112**, 9238 (2008).

[25] K. Ota, K. Koyasu, K. Ohshimo, and F. Misaizu, Chem. Phys. Lett. **588**, 63 (2013).

[26] R. H. A. del Toro, F. Aguilera-Granja, A. Vega, and L. C. Balbás, Phys. Chem. Chem. Phys. **16**, 21732 (2014).

[27] C. N. van Dijk, D. R. Roy, A. Fielicke, T. Rasing, A. C. Reber, S. N. Khanna, and A. Kirilyuk, Eur. Phys. J. D **68**, 357 (2014).

[28] K. Ohshimo, T. Komukai, R. Moriyama, and F. Misaizu, J. Phys. Chem. A **118**, 3899 (2014).

[29] C. J. Dibble, S. T. Akin, S. Ard, C. P. Fowler, and M. A. Duncan, J. Phys. Chem. A **116**, 5398 (2012).

[30] N. T. Tung, N. M. Tam, M. T. Nguyen, P. Lievens, and E. Janssens, J. Chem. Phys. **141**, 044311 (2014).

[31] S. Yin, W. Xue, X.-L. Ding, W.-G. Wang, S.-G. He, and M.-F. Ge, Int. J. Mass. Spectrom. **281**, 72 (2009).

[32] N. O. Jones, B. V. Reddy, F. Rasouli, and S. N. Khanna, Phys. Rev. B **72**, 165411 (2005).

[33] M. Ju, J. Lv, X.-Y. Kuang, L.-P. Ding, C. Lu, J.-J. Wang, Y.-Y. Jin, and G. Maroulis, RSC Adv. **5**, 6560 (2015).

[34] G. L. Gutsev, K. G. Belay, K. V. Bozhenko, L. G. Gutsev, and B. R. Ramachandran, Phys. Chem. Chem. Phys. **18**, 27858 (2016).

[35] H. T. Pham, N. T. Cuong, N. M. Tam, V. D. Lam, and N. T. Tung, Chem. Phys. Lett. **643**, 77 (2016).

[36] R. Logemann, G. A. de Wijs, M. I. Katsnelson, and A. Kirilyuk, Phys. Rev. B **92**, 144427 (2015).

[37] R. Logemann, A. N. Rudenko, M. I. Katsnelson, and A. Kirilyuk, Phys. Rev. Mater. **2**, 073001 (2018).

[38] W. Jin, C. Li, G. Lefkidis, and W. Hübner, Phys. Rev. B **89**, 024419 (2014).

[39] C. Li, W. Jin, H. P. Xiang, G. Lefkidis, and W. Hübner, Phys. Rev. B **84**, 054415 (2011).

[40] W. Hübner, S. Kersten, and G. Lefkidis, Phys. Rev. B **79**, 184431 (2009).
[41] N. Zhang, H. Du, J. Chang, W. Jin, C. Li, G. Lefkidis, and W. Hübner, Phys. Rev. B **98**, 104431 (2018).
[42] H. Du, J. Liu, N. Zhang, J. Chang, W. Jin, C. Li, G. Lefkidis, and W. Hübner, Phys. Rev. B **99**, 134430 (2019).
[43] M. J. Frisch, G. W. Trucks, H. B. Schlegel, G. E. Scuseria, M. A. Robb, J. R. Cheeseman, G. Scalmani, V. Barone, G. A. Petersson, H. Nakatsuji, X. Li, M. Caricato, A. V. Marenich, J. Bloino, B. G. Janesko, R. Gomperts, B. Mennucci, H. P. Hratchian, J. V. Ortiz, A. F. Izmaylov, J. L. Sonnenberg, D. Williams-Young, F. Ding, F. Lipparini, F. Egidi, J. Goings, B. Peng, A. Petrone, T. Henderson, D. Ranasinghe, V. G. Zakrzewski, J. Gao, N. Rega, G. Zheng, W. Liang, M. Hada, M. Ehara, K. Toyota, R. Fukuda, J. Hasegawa, M. Ishida, T. Nakajima, Y. Honda, O. Kitao, H. Nakai, T. Vreven, K. Throssell, J. A. Montgomery, Jr., J. E. Peralta, F. Ogliaro, M. J. Bearpark, J. J. Heyd, E. N. Brothers, K. N. Kudin, V. N. Staroverov, T. A. Keith, R. Kobayashi, J. Normand, K. Raghavachari, A. P. Rendell, J. C. Burant, S. S. Iyengar, J. Tomasi, M. Cossi, J. M. Millam, M. Klene, C. Adamo, R. Cammi, J. W. Ochterski, R. L. Martin, K. Morokuma, O. Farkas, J. B. Foresman, and D. J. Fox, *Gaussian 16, Revision B.01* (Gaussian, Inc., Wallingford, CT, 2016).
[44] X. F. Lin, Y. Y. Xi, and J. Sun, J. Phys. Chem. C **116**, 3503 (2012).
[45] L.-S. Wang, H. B. Wu, and S. R. Desai, Phys. Rev. Lett. **76**, 4853 (1996).
[46] Y. Pavlyukh, E. Rentschler, H. J. Elmers, W. Hübner, and G. Lefkidis, Phys. Rev. B **99**, 144418 (2019).
[47] H. Nakatsuji, Chem. Phys. Lett. **67**, 329 (1979).
[48] S. Koseki, M. W. Schmidt, and M. S. Gordon, J. Phys. Chem. A **102**, 10430 (1998).
[49] T. Hartenstein, C. Li, G. Lefkidis, and W. Hübner, J. Phys. D: Appl. Phys. **41**, 164006 (2008).
[50] B. W. Shore, *Manipulating Quantum Structures Using Laser Pulses* (Cambridge University Press, Cambridge, 2011).
[51] G. Lefkidis and W. Hübner, Phys. Rev. B **76**, 014418 (2007).
[52] Y. Pavlyukh, W. Hübner, and G. Lefkidis, Phys. Rev. B **100**, 054444 (2019).
[53] G. Lefkidis and W. Hübner, Phys. Rev. B **87**, 014404 (2013).